# Supporting Information

## An Enhanced Couette Flow Printing Strategy to Recover the Efficiency Losses by Area and Substrate Differences in Perovskite Solar Cells

*Chenxiang Gong, Baojin Fan, Feng Li, Zhi Xing, Xiangchuan Meng, Ting Hu, Xiaotian Hu* and Yiwang Chen**

Keywords: Patterned-meniscus coating, Couette flow, Colloidal particles, Flexible Perovskite solar cells, Efficiency loss

## Experimental Section

### Materials

All the chemical materials and reagents are purchased and used directly without further optimization or purification. anhydrous N, N-dimethylformamide (DMF, Sigma-Aldrich), PEDOT:PSS (CLEVIOS$^{TM}$ PH1000, Heraeus), Zincdi[bis(trifluoromenthylsulfonyl) imide](Zn(TFSI)$_2$, Sigma-Aldrich), lead (II) iodide ($PbI_2$, 99.999% purity, Alfa Asear), cesium iodide (CsI, Xi'an p-OLED Corp), methanaminium bromide (MABr, Xi'an p-OLED Corp), formamidinium iodide (FAI, Xi'an p-OLED Corp), aqueous PEDOT:PSS solution (CLEVIOS$^{TM}$ Al4083, Heraeus), methylammonium chloride (MACl, Xi'an p-OLED Corp), tin(IV) oxide ($SnO_2$, Alfa Asear), lithium bis(trifluoromethylsulfonyl) imide (Li-TFSI, >98% purity, Alfa Asear), 2,2',7,7'-Tetrakis [N, N-di(4-methoxyphenyl) amino]-9,9'-spirobifluorene (spiro-OMeTAD, 99% purity, Luminescence Technology Crop).

### Preparation of the stretchable transparent electrode.

To achieve a high ductility transparent electrode without affecting the conductivity under extreme deformation. Both the bottom and top electrode employed the high conductive PEDOT:PSS (hc-PEDOT:PSS)[1]. PEDOT:PSS (PH1000) with 20 mg/ml Zincdi[bis(trifluoromenthylsulfonyl) imide] (Zn(TFSI)$_2$) dropping were mixed together. After that, the modification ink was slot-die coated on the PDMS substrates via optimized shear stress. The sheet resistance of modification PEDOT:PSS electrode is about 17 Ω/□. To fabricate flexible devices by meniscus-coating, the PEDOT:PSS electrode film was fabricated by meniscus-coating (the blading speed are 5, 15, 25 and 30 mm $s^{-1}$ and the distance between meniscus and substrate is 40 μm). Substrate temperature was also considered as a variable condition, here, we choose the specific temperature is 50 $^{o}$C as the optimal condition.

### The lift-off processes.

The preparation process of perovskite film is identical to the conventional sample preparation technology. Initially, the polystyrene (PS, 20 mg $ml^{-1}$, in CB) solution was blade-coated onto the pre-cleaned substrates at 10 mm/s shear rate, and dried naturally at room temperature for 10 min in a $N_2$-filled glove box. Then the 30 μl of DMF was blade-coated on top of the PS-based substrates to enhance the wettability of the PS films upon which perovskites ink deposited. Secondly, the perovskite films were deposited on the PS-based substrates, the samples based on the PS film were soaked into the CB solvent for 30 min at room temperature. To ensure that PS film can be fully dissolved, the PS film cannot undergo

thermal annealing treatment, the porous structure of naturally dried PS film can provide better solvent dissolution conditions. Then, the PS film was completely dissolved by the CB, the perovskite film will be detached from the substrate and floated in CB solvent. Subsequently, the successfully lift-off perovskite film is flipped to expose the bottom surface and transferred by a clean substrate. Ultimately, to obtain the non-residual perovskite bottom surface, the surface needs to be washed more than three times by CB to remove residual PS components.

**Fabrication of the perovskite solar cells**

The perovskite precursor solution is prepared by dissolving 742.2 mg $PbI_2$, 19.8 mg CsI, 224.4 mg FAI, 20.3 mg MACl and 16.2 mg MABr in 0.8 mL anhydrous DMF and 0.2 mL anhydrous DMSO mixture solvent in glovebox. The perovskite precursor solution is meniscus-coated on the electron transport layer (ETL) coated substrates. Before the perovskite film is annealed, it needs to be vacuum pretreated (vacuum degree below 200 Pa, lasting two minutes). Then, the perovskite precursor coated substrate is annealed on a hot plate at 150 ℃ for 30 min. Subsequently, the spiro-OMeTAD is deposited by meniscus-coating. On the contrary, in the flexible device fabrication process, the top PEI/PEDOT:PSS/PDMS electrode was deposited via a film-transfer lamination technique[2].

**Film characterizations**

The ultraviolet-visible (UV-Vis) spectra were represented on a SHIMADZU, UV-2600 spectrophotometer. Kelvin probe force microscopy (KPFM) was measured by nano-scope multimode (Bruker). For the ultraviolet photoemission spectroscopy (UPS) measurements, He I (21.22 eV) radia-tion line from a discharge lamp was used, with an experi-mental resolution of 0.15 eV. The morphology of films was measured by AFM (nano-scope multimode Bruker) and SEM (JEOL, JSM-7500F, 104 Japan) at an accelerating voltage of 5.0 KV. To measure the absorption or transmittance properties for the electrode or perovskite layers, the ultraviolet-visible spectra (UV-vis, SHIMADZU, UV-2600 spectrophotometer) is conducted. *X*-ray diffraction (XRD) was recorded by using a D8-Discover 25 diffractometer (Bruker). Steady-state photoluminescence (PL) and time-resolved photoluminescence (TRPL) surveyed at the peak emission of ~770 nm (on the excitation at 550 nm) are carried out by the steady state and lifetime spectrometer (FLS920, Edin-burgh Instruments Ltd). The dual-beam ToF-SIMS depth profiling measurements were executed on a ToF-SIMS 5 instrument (ION-TOF GmbH) in an interlaced mode. The electrical impedance spectroscopy (EIS) is performed with Zahner electrochemi-cal workstation. The SCLC is described by $J = (9/8)\varepsilon_0\varepsilon r\mu h$ (V2/D3),

where $\varepsilon_0$ is the vacuum dielectric con-stant, μh is the hole mobility, V is the voltage drop across the device, and D is the hole interface layer thickness. XPS studies were performed on a Thermo-VG Scientific ESCALAB 250 photoelectron spectrometer using a monochromated AlKa (1486.6 eV) *X*-ray source. All recorded peaks were corrected for electrostatic effects by setting the C-C component of the C 1s peak to 284.8 eV.

**Solar cells characterizations**

The current density-voltage *(J-V)* curves are characterized using Keithley 2400 source-meter. The currents are measured under the solar simulator (Enli Tech, 100 mW $cm^{-2}$, AM 1.5 G irradiation). All the measurements are executed under nitrogen with room temperature. The reverse scan range is from 1.3 V to 0 V and the forward scan range is 0 V to 1.3 V, with 8.0 mV for each step, the scan rate is 0.2 V $s^{-1}$, the delay time is 30 ms, respectively. The incident photo-to-electron conversion efficiency spectra (IPCE) are detected under monochromatic illumination (Oriel Cornerstone 260 1/4 m monochromator equipped with Oriel 70613NS QTH lamp), and the calibration of the incident light is performed with a monocrystalline silicon diode. The repeated bending cycle tests are inspected by a custom-made stretching machine, and it's actuated by a stepper motor (Beijing Zhongke J&M). The results of every bending investigate averaged measurements data all come from more than 60 samples.

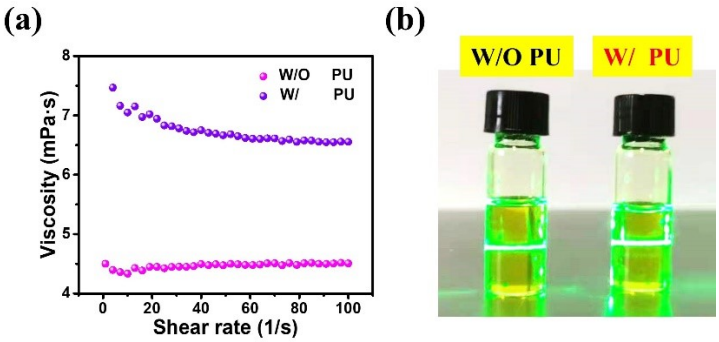


**Figure S1.** The viscosity characterization of perovskite precursor ink with and without PU. (b) Optical images of both perovskite precursor ink, and an obvious Tyndall effect can be seen under a green laser.

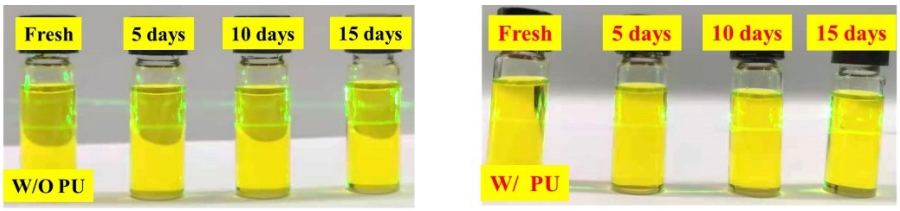


**Figure S2.** The Tyndall effect is used to detect the change of colloidal particle size with aging time of perovskite precursor inks.

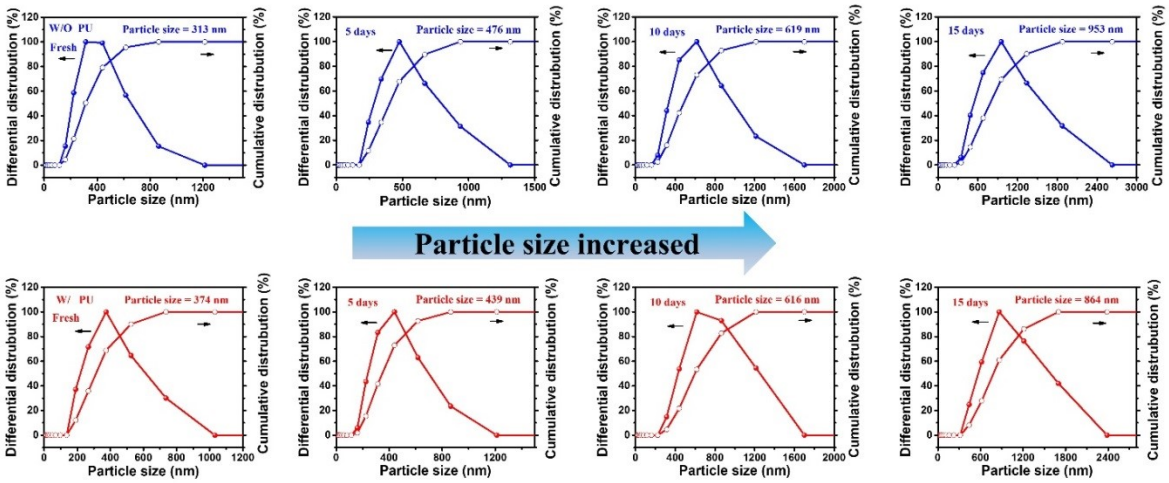


**Figure S3.** The particle size distribution of colloidal particles with aging time of perovskite precursor inks (from fresh to 15 days of aging time).

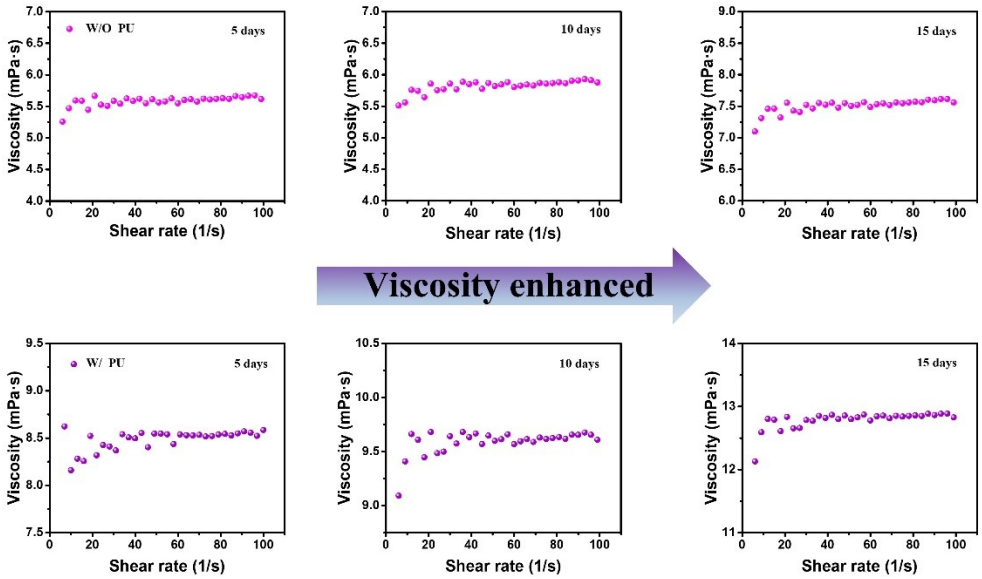


**Figure S4.** The viscosity performance of perovskite precursor inks with 15 days of aging time.

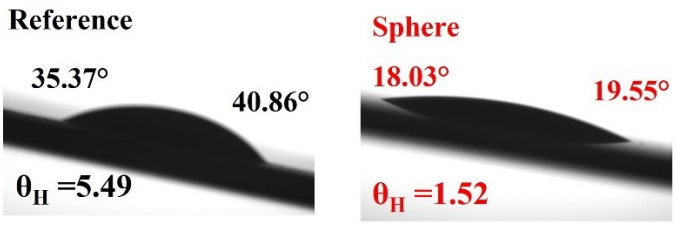


**Figure S5.** Characterization of viscous performance on FSS and PSS.

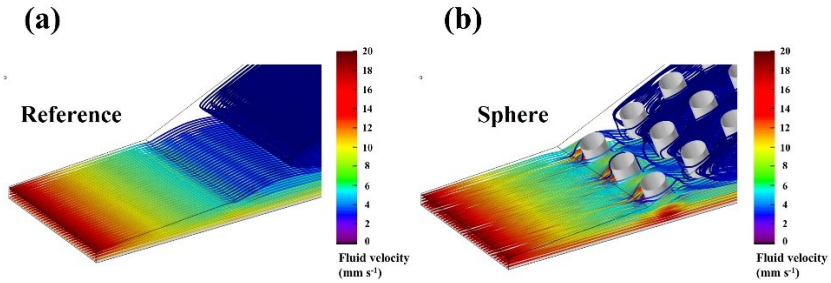


**Figure S6.** The simulation images of motion state of perovskite precursor inks in FSS and PSS coating process.

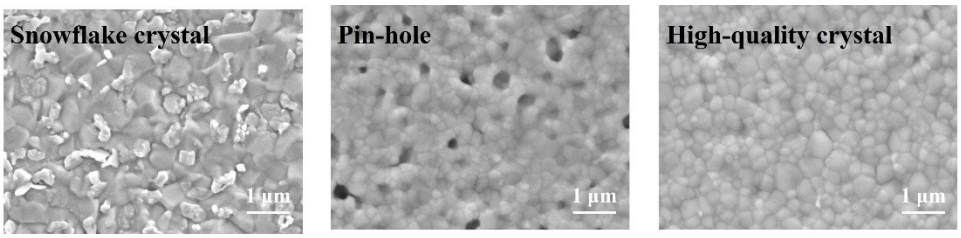


**Figure S7.** The SEM images of perovskite films based on different shearing-rate (slit-width) variates.

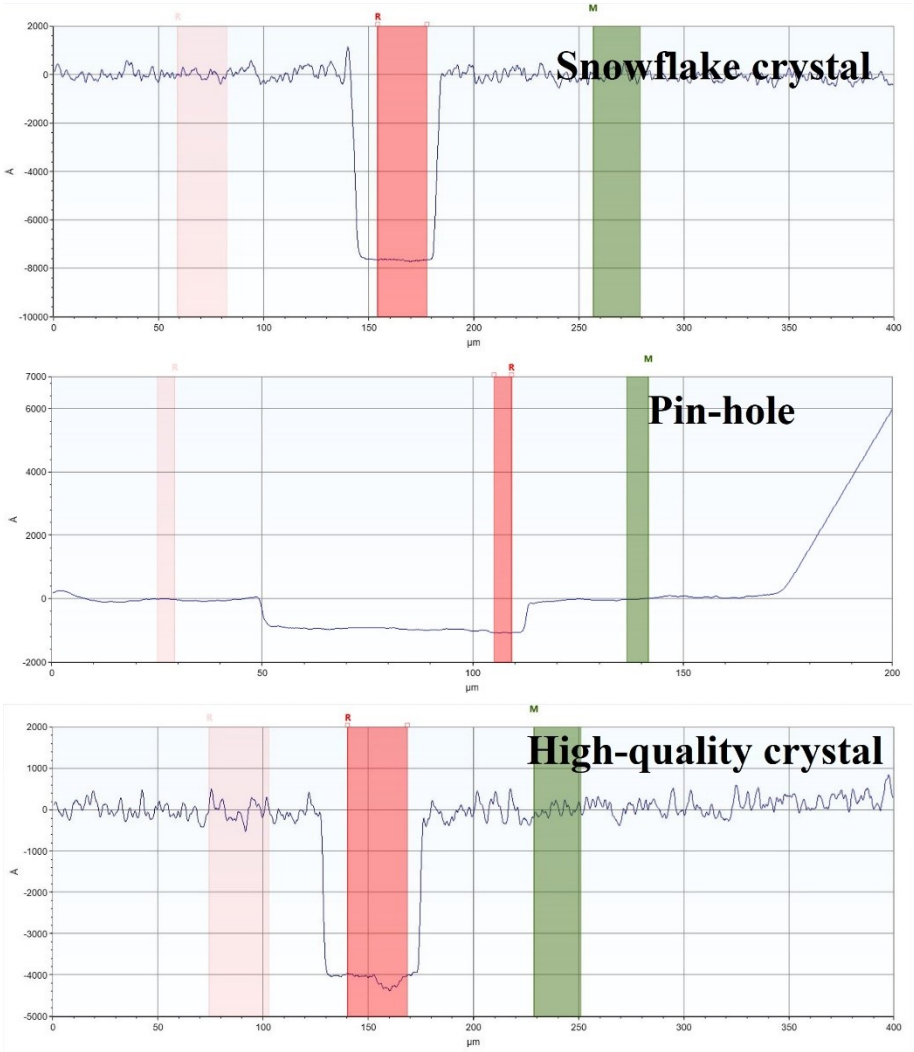


**Figure S8.** The film thickness of the corresponding perovskite films.

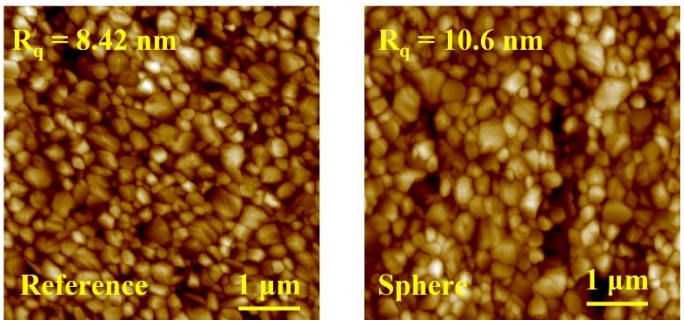


**Figure S9.** The AFM images of patterned-meniscus coating for perovskite films with non-additive precursor ink.

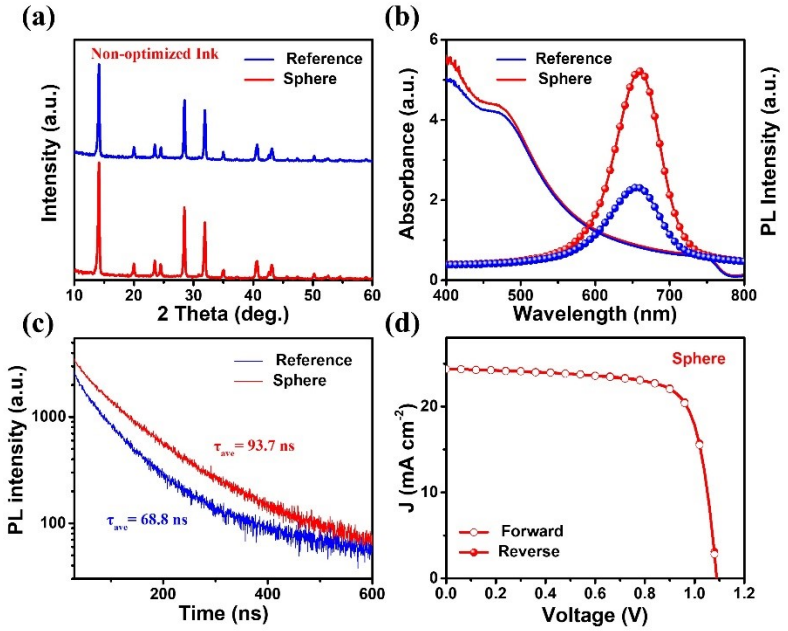


**Figure S10.** (a) XRD patterns, (b) UV-vis absorption spectra and the steady-state photoluminescence spectra, (c) TRPL spectra of perovskite films, and (d) *J-V* curves of perovskite solar cells (employing non-optimized perovskite precursor ink fabrication).

The crystals quality of corresponding perovskite film can be improved by employing patterned-meniscus coating, as shown in AFM images (Fig. S9) and XRD patterns (Fig. S10a). Moreover, the improvement of crystal quality can also be reflected in the of optical performances. As shown in Fig. S10b and S10c, all the UV-vis absorption spectrum, PL and TRPL characterizations intuitively exhibit optical performance improvements, manifesting patterned-meniscus coating process universality to inhibit colloidal agglomeration in perovskite precursor ink. Furthermore, the hysteresis effect of corresponding devices has been further reduced via the PSS process, which is consistent with previous discussed results (Fig. S10d).

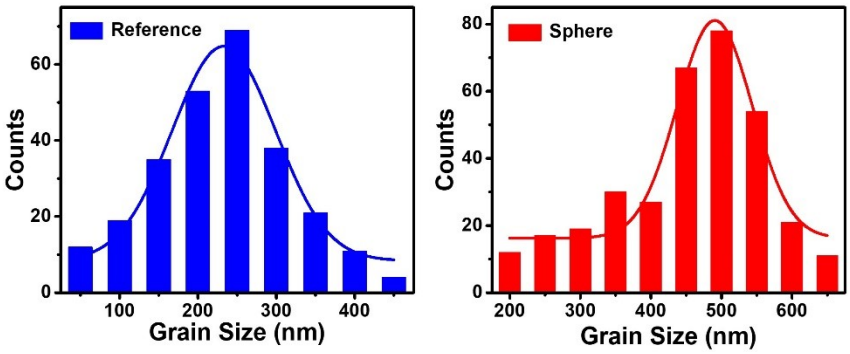


**Figure S11.** The grain distribution of corresponding perovskite films.

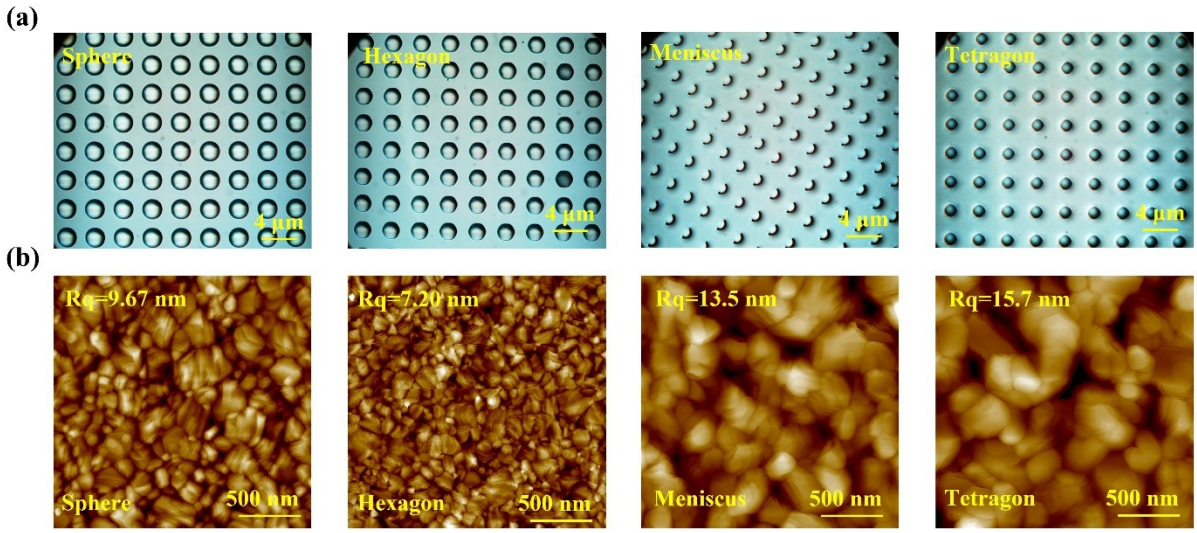


**Figure S12.** (a) The optical images of four different patterns of silicon slice. (b) The AFM images of the corresponding perovskite film by different silicon slice patterns.

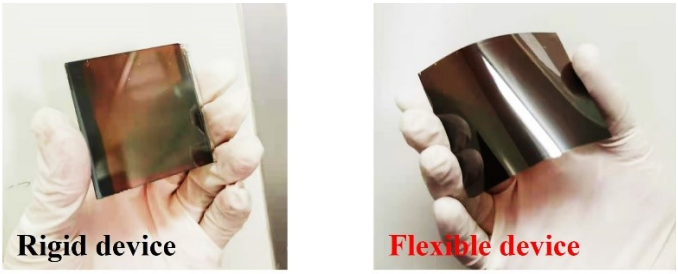


**Figure S13**. The corresponding images of perovskite films via patterned-meniscus coating.

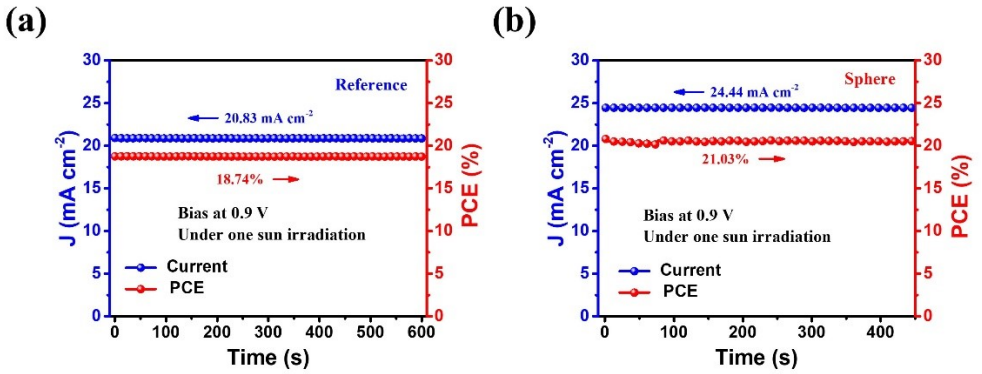


**Figure S14**. Stabilized output power and photocurrent of the PSCs with (a) FSS and (b) PSS processes measured under a constant bias voltage (0.9 V) near the maximum power point.

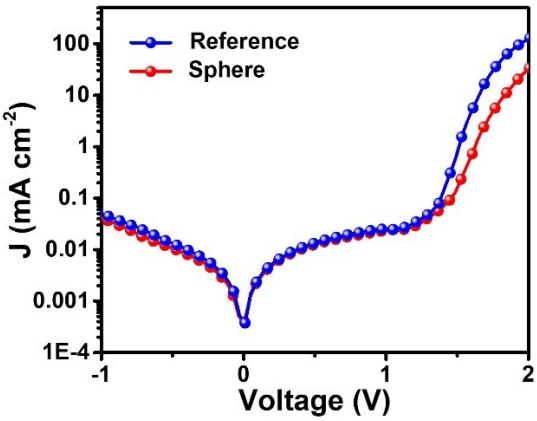


**Figure S15.** Dark *J-V* curves of patterned-meniscus coating for perovskite solar cells.

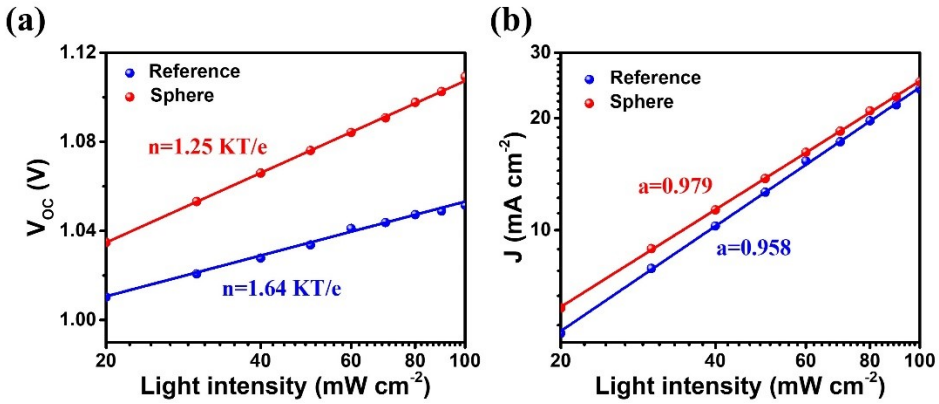


**Figure S16.** $V_{oc}$ and $J_{sc}$ dependence of the PSCs via patterned-meniscus coating at various illumination intensities.

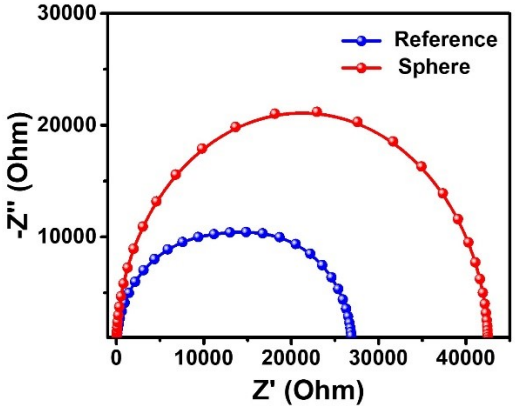


**Figure S17.** EIS of corresponding device based on patterned-meniscus coating fabrication.

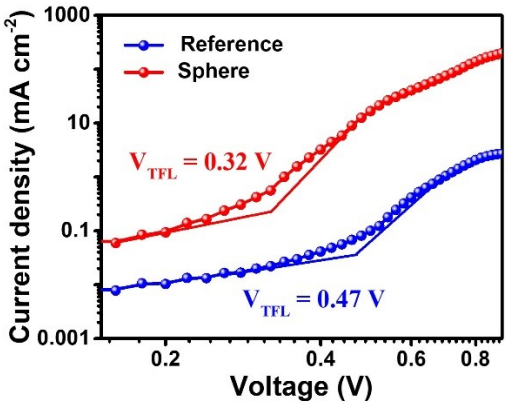


**Figure S18.** The *J-V* curves by the SCLC pattern of the device via patterned-meniscus coating process.

The space-charge-limited-current (SCLC) pattern can investigate the trap density ($n_{trap}$) of perovskite films. The $n_{trap}$ can be calculated by the relevant equation[3]:

$$n_{trap} = \frac{2V_{tfl}\varepsilon\varepsilon_0}{eL^2}$$

Here $V_{tfl}$ is the trap-filled limited voltage and the value of with patterned-meniscus coating and reference devices is 0.32 V and 0.47 V, $\varepsilon_0$ is the vacuum dielectric constant, the L (~ 400 nm) is the thickness of perovskite films, $\varepsilon$ (nearly 32) is the relative dielectric constant of perovskite films and e ($1.6 \times 10^{-19}$) is the elementary charge. Therefore, the trap density ($n_{trap}$) calculated with patterned-meniscus coating and reference devices are $7.1 \times 10^{14}$ $cm^{-3}$ and $1.04 \times 10^{15}$ $cm^{-3}$, respectively.

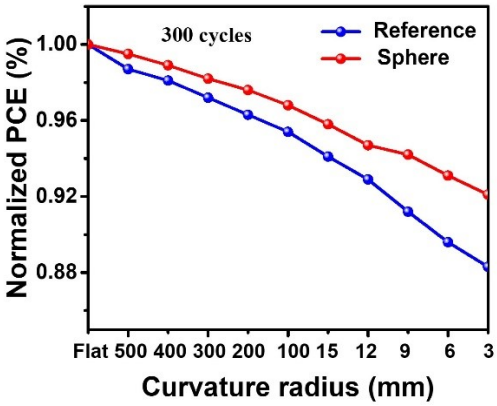


**Figure S19.** Normalized averaged PCE value for the flexible PSCs after bending 300 cycles with different bending radius.

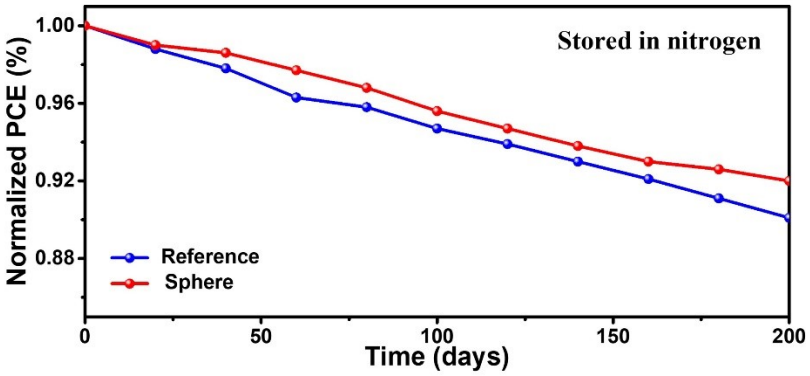


**Figure S20.** Long-term stability of devices over 200 days stored in the $N_2$ glovebox condition.

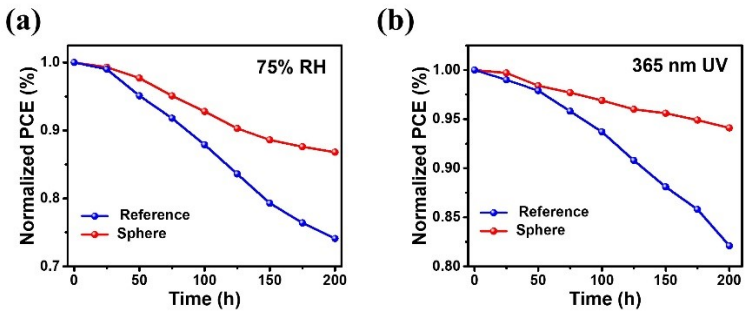


**Figure S21.** The normalized PCE decay curves of the PSCs (a) under a 75% humidity and (b) under 365 nm UV irradiation for 200 h.

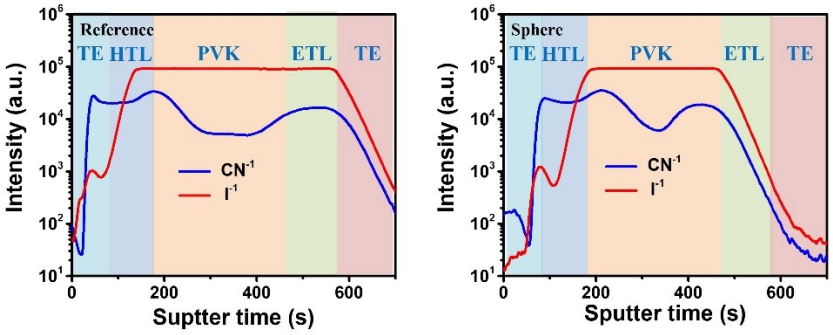


**Figure S22.** Tof-SIMS elemental depth profiles for the PSCs via reference and sphere fabrication.

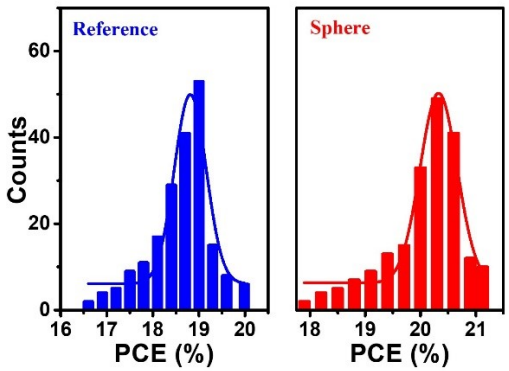


**Figure S23.** The corresponding PCE distributions.

**Table S1.** The parameters derived from the *J-V* curves of flexible PSCs.

| Silicon slice shape | Area ($cm^2$) | $J_{SC}$ (mA $cm^{-2}$) | $V_{OC}$ (V) | FF (%) | PCE (%) |
|---|---|---|---|---|---|
| **Reference** | 0.04 | 22.96 | 1.08 | 76.21 | 18.90 |
| | 0.1 | 24.34 | 1.04 | 72.06 | 18.24 |
| | 0.2 | 24.48 | 1.03 | 68.98 | 17.39 |
| | 0.3 | 22.68 | 1.00 | 73.17 | 16.59 |
| | 0.4 | 21.94 | 1.04 | 69.89 | 15.95 |
| | 0.5 | 22.38 | 1.09 | 61.64 | 15.04 |
| | 0.6 | 23.69 | 0.98 | 58.69 | 13.63 |
| | 0.7 | 21.97 | 1.07 | 55.12 | 12.96 |
| | 0.8 | 18.06 | 1.04 | 63.85 | 11.99 |
| | 0.9 | 17.11 | 0.98 | 63.42 | 10.63 |
| | 1.01 | 18.33 | 1.12 | 47.67 | 9.79 |
| **Sphere** | 0.04 | 24.62 | 1.09 | 74.83 | 20.08 |
| | 0.1 | 24.36 | 1.09 | 75.00 | 19.91 |
| | 0.2 | 23.36 | 1.08 | 75.45 | 19.04 |
| | 0.3 | 25.10 | 1.05 | 68.74 | 18.12 |
| | 0.4 | 24.05 | 1.07 | 69.55 | 17.90 |
| | 0.5 | 21.42 | 1.10 | 72.79 | 17.15 |
| | 0.6 | 22.99 | 1.05 | 68.03 | 16.42 |
| | 0.7 | 23.22 | 1.06 | 64.81 | 15.95 |
| | 0.8 | 22.79 | 0.85 | 78.71 | 15.25 |
| | 0.9 | 22.67 | 1.08 | 61.02 | 14.94 |
| | 1.01 | 18.97 | 1.05 | 71.31 | 14.20 |

**Table S2.** The parameters derived from the *J-V* curves of PSCs based on the rigid substrate.

| Silicon slice shape | Area ($cm^2$) | $J_{SC}$ (mA $cm^{-2}$) | $V_{OC}$ (V) | FF (%) | PCE (%) |
|---|---|---|---|---|---|
| **Reference** | 0.04 | 24.36 | 1.09 | 75.29 | 19.99 |
| | 0.1 | 24.48 | 1.08 | 74.00 | 19.56 |
| | 0.2 | 23.25 | 1.08 | 74.97 | 18.82 |
| | 0.3 | 25.40 | 1.03 | 70.08 | 18.33 |
| | 0.4 | 23.61 | 1.09 | 68.76 | 17.70 |
| | 0.5 | 23.25 | 1.04 | 70.72 | 17.10 |
| | 0.6 | 21.59 | 1.07 | 69.88 | 16.14 |
| | 0.7 | 21.16 | 1.02 | 70.12 | 15.13 |
| | 0.8 | 19.61 | 1.04 | 68.92 | 14.06 |
| | 0.9 | 18.52 | 1.02 | 71.92 | 13.59 |
| | 1.01 | 20.83 | 0.97 | 64.58 | 13.05 |
| **Sphere** | 0.04 | 24.86 | 1.14 | 74.55 | 21.12 |
| | 0.1 | 25.38 | 1.12 | 72.64 | 20.65 |
| | 0.2 | 24.87 | 1.09 | 74.60 | 20.22 |
| | 0.3 | 25.69 | 1.08 | 72.84 | 20.21 |
| | 0.4 | 25.11 | 1.12 | 70.93 | 19.95 |
| | 0.5 | 24.40 | 1.09 | 72.84 | 19.37 |
| | 0.6 | 23.59 | 1.08 | 74.90 | 19.08 |
| | 0.7 | 25.47 | 1.05 | 70.72 | 18.91 |
| | 0.8 | 24.32 | 1.03 | 74.08 | 18.56 |
| | 0.9 | 24.88 | 1.06 | 70.10 | 18.49 |
| | 1.01 | 24.37 | 1.09 | 69.48 | 18.46 |

**Table S3.** The summary of PCE loss in different literatures.

| Device | PCE loss (%) | Scale ($cm^2$) | Source |
|---|---|---|---|
| Rigid | 23.7 | 0.09 $cm^2$ to 0.7 $cm^2$ | Energy Environ. Sci. 2017, 10, 145-152 |
| | 16 | 0.0754 $cm^2$ to 1 $cm^2$ | Small 2018, 15, 1804005 |
| | 4.8 | 0.09 $cm^2$ to 1 $cm^2$ | Joule 2019, 3, 402-416 |
| | 7.2 | 0.09 $cm^2$ to 1 $cm^2$ | Joule 2021, 5, 958-974 |
| | 14.4 | 0.04 $cm^2$ to 1 $cm^2$ | Adv. Sci. 2020, 7, 2000480 |
| This work | 12.6 | 0.04 $cm^2$ to 1 $cm^2$ | - |
| Flexible | 32.9 | 2.01 $cm^2$ to 25 $cm^2$ | Joule 2019, 3, 2205-2218 |
| | 17.7 | 1.01 $cm^2$ to 9.33 $cm^2$ | Energy Environ. Sci., 2019,12, 979-987 |
| | 24 | 0.16 $cm^2$ to 1.4 $cm^2$ | Adv. Energy Mater., 2018, 8, 1702915 |
| | 14.5 | 0.1 $cm^2$ to 1 $cm^2$ | Adv. Sci., 2019, 6, 1901067 |
| This work | 29.3 | 0.04 $cm^2$ to 1 $cm^2$ | - |

**Reference**

[1] X. Hu, X. Meng, L. Zhang, Y. Zhang, Z. Cai, Z. Huang, M. Su, Y. Wang, M. Li, X. Yao, F. Wang, W. Ma, Y. Chen, Y. Song, *Joule* **2019,** *3,* 2205-2218.

[2] Y. Zhou, C. Fuentes-Hernandez, J. Shim, J. Meyer, A. J. Giordano, H. Li, P. Winget, T. Papadopoulos, H. Cheun, J. Kim, M. Fenol, A. Dindar, W. Haske, E. Najafabadi, T. M. Khan, H. Sojoudi, S. Barlow, S. Grham, J. B. Brédas, S. R. Marder, A. Kahn, B. Kippelen, *Science* **2012**, *336,* 327-332.

[3] Q. Dong, Y. Fang, Y. Shao, P. Mulligan, J. Qiu, L. Cao, J. Huang, *Science* **2015,** *347*, 967-970.